THE JOURNAL OF PHYSICAL CHEMISTRY A

Article

Cite This: J. Phys. Chem. A 2019, 123, 8036−8042

pubs.acs.org/JPCA

Polymer Patterning with Self-Heating Atomic Force Microscope Probes

H. Tunc Ciftci,[†] Laurent Pham Van,[‡] Bert Koopmans,[†] and Oleg Kurnosikov*[,†]

[†]Eindhoven University of Technology, Eindhoven 5600 MB, The Netherlands

[‡]Centre CEA de Saclay, Gif-sur-Yvette 91191, France

Supporting Information

ABSTRACT: Scanning probe-assisted patterning methods already demonstrated a high degree of capabilities on submicrometer scales. However, the throughput is still far from its potential because of complexity or fragility of the probes for exploiting thermal effects, chemical reactions, and voltage-induced processes in various patterning operations. Here, we present a new approach to thermomechanical patterning by implementing a multitasking atomic force microscopy (AFM) probe: the functionalized planar probes. In this method, we can generate a tunable thermal gradient between the tip and the sample, wherein they remain in the noncontact regime. In principle, the capillary instability provoked by the van der Waals interaction yields a pull-off force toward the tip. Hence, locally rising protrusions form features at any selected position on a polymer surface without any chemical reaction or irreversible transformation. These multitasking probe-integrated AFMs can pave the way for a remarkable freedom in determining the operation regime on submicrometer surface-patterning applications.

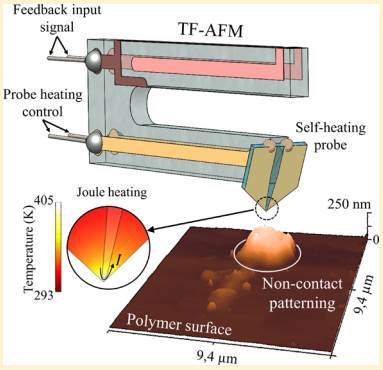

INTRODUCTION

Atomic force microscopy (AFM) is already beyond being just an extensively used imaging and characterization method because it can also function as a tool for surface manipulation and patterning on submicrometer scales. The advent of probe-assisted surface tailoring, known as scanning probe lithography (SPL),[1] opened the way for advanced surface tailoring of various materials either reversible or irreversible. Particularly, an SPL application named as AFM-assisted polymer patterning governed by the material accumulation or dissipation by mass transport over thermally softened polymer surfaces is an example of such reversible patterning. It is locally controlled by tuning capillary effects and van der Waals forces in the region between the tip and the sample (Figure 1).

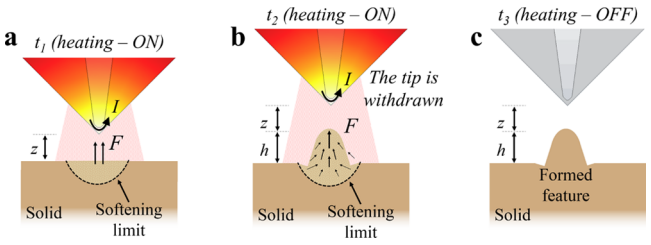

Figure 1. (a) Heat dissipation from the tip softens a volume of the paraffin surface, and then, (b) pull-off force (F) raises a protrusion toward the probe in the presence of local instability, while the feedback control is still on. This provisional protrusion (c) solidifies rapidly when the heating is switched off and forms a surface feature on the paraffin surface.

In this paper, we report a new and reliable implementation of the AFM-assisted polymer patterning process with a hot AFM probe in the noncontact regime. To get this functionality, we have developed planar AFM probes suitable for the temperature control. Using this method, the surface patterning consist of two steps: the creation of surface instability of the locally softened polymer (Figure 1a,b)., and freezing the resulting surface feature after the tip heating is switched off (Figure 1c). Although the idea behind the SPL seems to be simply based on controllable tip−surface interaction at the phase transition of the polymer, so far, the successful AFM-assisted applications required complex add-on systems. For instance, AFMEN[2−4] carries out electrostatic nanolithography by heating up the whole sample externally in the presence of a strong electric field. On the other hand, MILLIPEDE[5,6] and its successor Nanofrazor[7] systems provide thermomechanical writing by pressing the heatable AFM tip locally on polymer surface for patterning indentations. However, significant structural changes on an entirely heated sample during phase transition or mechanically pressed indentations by a multiple hot-tip system obviously limit the operations with shape-memory polymers[8] in terms of compatibility, repeatability, and recoverability.

In our view, the combination of the principles of AFMEN and MILLIPEDE approaches, yielding surface protrusions by localized pull-off forces acting on the thermally activated surface, and indentations by pressing a hot tip in the surface,

Received: June 26, 2019
Revised: August 13, 2019
Published: August 14, 2019

DOI: 10.1021/acs.jpca.9b06056
J. Phys. Chem. A 2019, 123, 8036−8042

respectively, would have several advantages for a reliable AFM-assisted polymer patterning. Because a sharp tip is the ultimate component of an AFM, the idea behind our design is to concentrate the thermally induced activation influence only at the tip end. We therefore developed functionalized probes that can induce the instant rise of temperature reaching up to the glassing transition or melting of most polymers only at the very end of the tip provoking the phase transition of the polymer in a very constricted area of the sample. In contrast to the approaches mentioned above, this phase transition occurs under the tip but without any mechanical contact with it. On the other hand, our probes are able to operate under feedback control during the thermal activation, while the tip keeps oscillating with the frequency of 32 kHz in the noncontact regime. Therefore, this periodical close interaction under thermal activation can yield growth upward while preventing an undesired contact between the tip and the surface contrary to MILLIPEDE and Nanofrazor approaches.

The multitasking tip capable of thermal control at the tip without disfunctioning the force sensor due to overheating can be realized at efficient thermal decoupling of the tip and the force sensor. The traditionally used AFM tips are made of bulk silicone attached to a Si-based cantilever (Figure 2a) or small

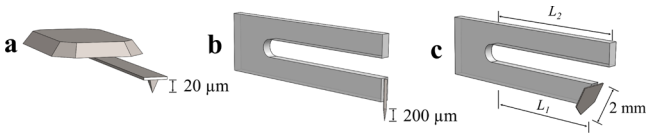

Figure 2. Traditional AFM probes: (a) conventional silicon-based cantilever with a conical tip (20 μm), (b) tuning fork force sensor with a needle-like tip (200 μm), and our new approach: (c) rebalanced tuning fork force sensor attached carrying an oversize probe (2 mm) with a relatively flat and wide surface, which is suitable for functionalization.

pieces of metallic wires glued on a quartz tuning fork force sensor (Figure 2b). Unfortunately, both are not suitable for any dedicated multilead connection neither for controlling the tip temperature nor feedback regulation during heating for a stable operation. The realization of this function requires: (1) tailoring of the conductive structure of the tip providing electrical access via auxiliary connection and (2) maximal decoupling at the force sensing system from thermoactive elements.

In principle, the first requirement can be provided by additional lithography of the probes as it has been done for a number of functionalized cantilevers[9] in order to get thermoresistive, Hall-probe, or electrochemical sensing. However, especially the thermal decoupling for high heat dissipating processes is a real problem for cantilever-based force sensors. Therefore, we made the choice for quartz tuning fork force sensors. For such configuration, the tailoring of the needle-like probe is also possible as, for example, realized in the scanning near-field optical microscopes[10] or electrochemical SPM.[11] Nevertheless, they are not efficient in use yet. Actually, the needle-like shape of the tip is the main obstacle for reliable structuring. With regard to this problem, in our approach, we replace the needle-like tips (Figure 2a,b) by the thin-film planar probes (Figure 2c) with extra tailoring: the functionalized planar probes (FPPs) conjugated with quartz tuning forks.

The FPP is a piece (up to 2 × 2 mm^2) of a chip with a very sharp corner which is used to scan the surface. The sharpness of this probe is good enough to obtain atomic resolution in STM as confirmed in our previous report.[12] We succeed to fix the FPP on a modified quartz tuning fork force sensor (Figure 2c) and utilize it also in AFM. The FPP can easily be tailored because it has planar geometry with a relatively wide and flat face. We fabricated two electrodes on the chip connected by a narrow conducting bridge near the tip end. By driving current through this structure, we are able to generate a local temperature gradient at the tip apex. Therefore, we can simultaneously induce local heating such as in MILLIPEDE,[5,6] and the interaction force control between the tip and the softened surface such as in AFMEN.[2−4] The details of our technique are described in the Methods section.

Another essential ingredient of the FPP approach is rebalancing the total load effecting two prongs of the tuning fork. The FPP design can provide a wide and flat face for extra tailoring; however, this also means extra load effecting the probe-carrying prong with its large size (Figure 2c) as compared with the conventional needle-like probes (Figure 2a,b). This asymmetry in the shape yields a remarkable suppression in the oscillation of the extra-loaded prong, hence, a sharp decrease in the sensitivity as well. Within our approach, to a large extent, the successful AFM application is obtained due to the rebalancing of tuning fork resonators. The rebalancing restores the high Q-factor and provides high sensitivity to the atomic-scale forces. This aspect is discussed more detail in the Methods section.

In this study, we aimed to reveal the probe-assisted thermomechanical patterning in the surface morphology of paraffin wax with our FPPs. Paraffin wax is a well-known material with well-determined phase-transition parameters.[13] Therefore, paraffin is a very suitable material to prove the reliability of our functionalized probes and its applicability to a broader range of polymers.

METHODS

For demonstration, we decided to use a paraffin sample, which is a simple crystalline polymer. It has glass transition (T_g), a cold crystallization peak (T_{cc}), and a melting peak (T_m) temperatures at 309, 318.7, and 330.6 K, respectively.[13] In order to obtain the flat surface for thermomechanical patterning, we cover one face of flat glass by vaporizing paraffin wax in an oven which was heated up to 625 K.

As claimed, we are presenting the approach, where the tip will be formed with a planar structure. The fabrication and utilization of this structure in AFM is achieved by these main steps: the thin-film tailoring on the cleaved probe, forming a sharp tip, conjunction with the force sensor, electrical leads, the resolution test, and optimal control of the FPP.

We started probe fabrication with obtaining conductance across the probe in order to provide current-driven heating by FPP. We first deposited metallic Ta/Pt/AlO_x multilayer stacking on a well-insulating silica glass (Figure 3a).

Afterward, we formed a sharp tip by double cleaving a substrate as it was already demonstrated in our pilot study.[12] The sharp tip is formed at the intersection of propagating cleaving lines (Figure 3b,c).

Regarding where we formed the sharp tip, we tailored a metallic micro-/nanoconstriction on the conducting film (Figure 3d,e) by utilizing electroerosion to form a microbridge (Figure 3f) and FIB for a nanobridge (Figure 3g). In order to

DOI: 10.1021/acs.jpca.9b06056
J. Phys. Chem. A 2019, 123, 8036−8042

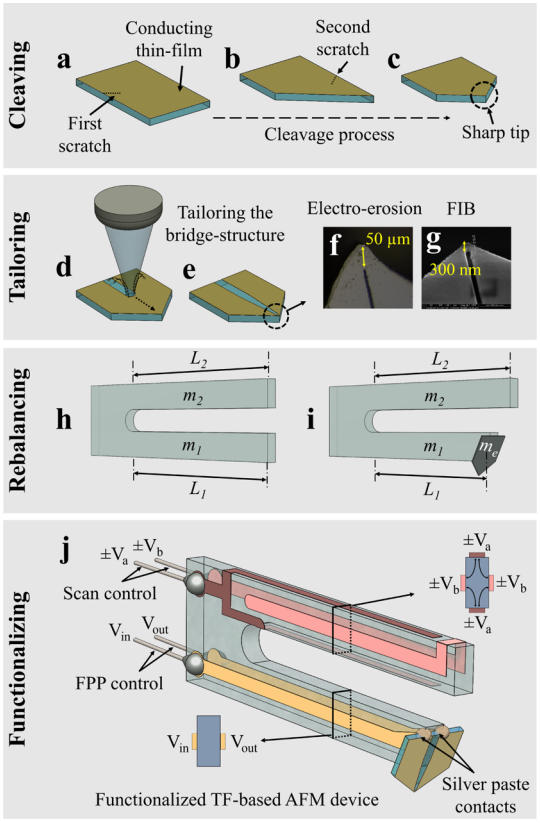

Figure 3. Schematics of each steps of the FPP fabrication. (a–c) Atomically sharp tip is formed at the intersection of the two cleaved sides. (d,e) Thin film is tailored close to the tip using (f) electroerosion and (g) focused ion beam (FIB) in order to form a bridge structure. (h) Two identical prongs of the tuning prong are (i) rebalanced by changing the length of the one carrying the extra mass (m_e). After all, (j) the leads on the prongs are modified. The upper prong with the bronze-colored leads are used to run scan and force sensing. The lower prong with the gold-colored leads are exploited to have electrical access to the tip end via silver paste.

functionalize this structure, we first prepared the force sensor to carry the FPP and then bonded them mechanically and electrically.

To obtain maximum detection performance from the force sensor with an oversize probe, we employed a stiff quartz tuning fork force sensor oscillating at 32.768 kHz (AB38T). The minimum detection force (F_{min}) of this sensor is expressed in terms of the spring constant (k), the resonant frequency (f_0), and the Q-factor (Q) as shown in eq 1.[14]

$$F_{min}\alpha \sqrt{\frac{k}{f_0 Q}} \tag{1}$$

As basically given above, high Q is essential for high sensitivity at low F_{min}. It is well known that an occurring asymmetry in the oscillation yields a sudden drop in the Q value.[14−18] Ng et al. have already explained how Q changes depending on Δm, which consist of the effective masses of the prongs (m_1 and m_2) and the extra mass (m_e) simply represented as $\Delta m = (m_1 + m_e) - m_2$.[18] In principle, we can rebalance our oscillator and regain high Q by holding Δm at approximately zero. Of course, we should take the prong lengths L_1 and L_2 into account because m_1 and m_2 directly rely to them with a direct proportion (Figure 3h,i).

However, we do not simply add extra mass onto the free ends of the prongs of a bare tuning fork. In our method, we change the length of one prong by removing a bit of the quartz material from the end. Therefore, we still expect a change in k, which depends on E, b, and L_1 or L_2, which are the Young's modulus, width, thickness, and length of a prong of the tuning fork, respectively, as given by eq 2.[14]

$$k = \frac{Ebh^3}{L_{1,2}^3} \tag{2}$$

According to (eq 2), a decrease in L_1 or L_2 yields an increase in k resulting in a variation of resonance frequency f_0. However, the sensitivity is mainly governed by the Q factor. This Q value is very critical to desymmetrization of the tuning fork, thus, the variation of L_1 or L_2. Nevertheless, it is possible to compensate this desymmetrization in L_1 and L_2 by rebalancing of the effective masses. We therefore performed an experiment revealing the relation between Δm, f_0, and Q.

The experimental results in Figure 4 reveal that rebalancing for an extra mass addition can recover high sensitivity because

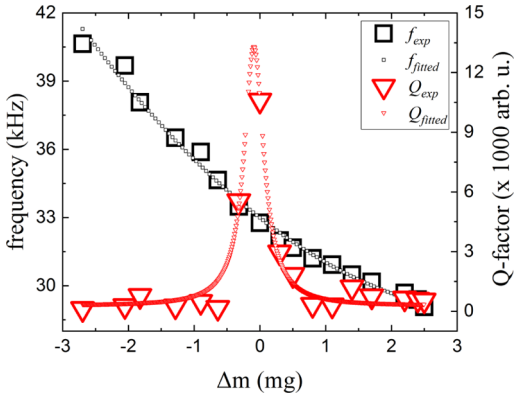

Figure 4. Oscillation and sensitivity characteristics of the tuning fork used in our system against change of effective mass on one prong.

the resulting Δm is approximately zero as assumed. Although the Q-factor is sufficiently high after rebalancing, it remains a little bit less than its default value. Actually, this offset between Q (after rebalancing) and Q_0 is not vitally disadvantageous.

Based on this experimental outcome, we polished away a certain amount of the quartz material from the end of one prong of the tuning fork, which would carry the FPP. In this step, we decreased m_1 by changing the length of the lower prong (L_1) by taking the extra mass (m_e) from the FPP into consideration (Figure 3h,i).

After this course adjustment, using a strong light cure adhesive drop (LOCTITE, 4305), we bonded FPP onto the shortened prong. Once the FPP and the prong are strongly conjugated, now, we process fine adjustment by gently polishing away some weight from inactive parts of the probe. At the end, because we fix the oscillation at 33 ± 1 kHz with the feedback signal via the leads on the upper prong (Figure 3j) by rebalancing prong loads as $m_2 \approx m_1 + m_e$, the resonator demonstrates a Q-factor value always in the range from 10^3 to 10^4 in ambient conditions. In order to obtain electrical access to the tip end via the leads on the lower prong, we applied silver paste (Holland Shielding Systems Bv, 3980 Shieldokit) (Figure 3j).

DOI: 10.1021/acs.jpca.9b06056
J. Phys. Chem. A 2019, 123, 8036−8042

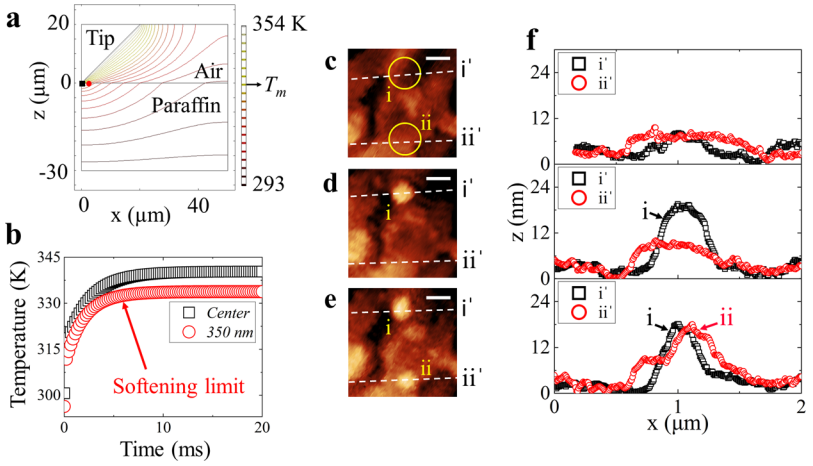

Figure 5. Plots obtained from our COMSOL model representing the (a) heat dissipation from the hot tip (at 354 K) to the paraffin wax through air, and the (b) instant thermal saturation of the softening limit at a radius of 350 nm, where the plots shown by the black squares and red circles represent the black and the red dots in (a). AFM nanographs taken from the paraffin sample represent the (c) two selected positions and their corresponding softening limit area circled in yellow and the thermomechanically patterned surface features (d) i and (e) ii, respectively. Scale bar in (c–e) is 500 nm. (f) Plots are taken from corresponding AFM images (c–e) in order to compare changing height characteristics along the *z*-axis before and after patterning.

To assess the resolution that the FPP can provide, we scanned a CoIrPt surface in order to determine the minimum detectable structure. The resolution appeared as ∼15 nm, which is sufficient for the thermomechanical polymer patterning (see the Supporting Information).

We optimized a reproducible cost-efficient hand-made FPP fabrication process explained above, which provides reliable working performance each time with sufficient sensitivity and tunable probe-surface interaction via electrical control at the tip end, such as temperature, without any need for an external source.

RESULTS AND DISCUSSION

In order to demonstrate the functionalization of our FPP tips, we present our results in the following way. First, we report a numerical modeling of temperature regimes of our FPP in order to get the concrete values of heating current through the probe and duration of thermal affection needed to locally melt the paraffin surface. In the modeling, the parameters in terms of dimension and material selection correspond to the real FPP probes that we fabricated which remained in the noncontact regime with the surface under ambient conditions. Then, we present the experimental results on growth of submicrometer protrusions on a paraffin surface with FPP probes to demonstrate the validity of our approach in general. Then, to gain insights in the mechanism of forming the surface protrusions, we provide additional experiments with higher heating power and report them in the last part of this section. Similar to the first part, we combined these additional experiments with numerical simulations.

In our experiments, in order to generate the thermal influence, we modulated the current flows through a ∼50 μm wide-tailored conductive bridge near the FPP tip end (Figure 1). It means that the heat dissipates along a small area where the current density is locally high. In order to estimate the set parameters necessary to soften a superficial area for submicrometric feature formation, we first modeled the time-dependent heat dissipation in this system using COMSOL.

Our model consists of the FPP with the real parameters of its geometry. For thermal calculations, we use the estimated mean tip–surface distance of 5 nm neglecting the oscillating behavior. According to this model, the temperature at the tip reaches up to 354 K when we drive 5 mA (Figure 5a). As a result of the heat dissipation in ambient conditions, an area on the paraffin surface lying just below this hot tip (the black dot in Figure 5a) instantly reaches up to ∼340 K and saturates at this level only in ∼5 ms as shown by the plot consisting of the black squares in Figure 5b. The outmost point that can reach up to 330.6 K, which is the melting temperature (T_m) of the paraffin wax used in this experiment, is 350 nm far from this center point (the red dot in Figure 5a). This distance defines our softening limit given by the plot consisting of the red circles in Figure 5b. In other words, we can melt an area with 700 nm of diameter on the paraffin surface in any selected position (Figure 5c).

The numerical modeling with COMSOL demonstrated convincing results by giving feasible set of parameters to realize thermomechanical patterning in our experiments. We performed our experiments using the exact values taken from the model and modified the paraffin surface without excessive trial-and-error attempts. As illustrated, Figure 5c shows the topography of the paraffin wax sample before thermomechanical patterning. As the cross-sections i′ and ii′ on the uppermost row in Figure 5f reveal, the operation area in Figure 5c has a roughness of approximately 5 nm. Again in Figure 5c, the indexes i and ii indicate the selected positions for the features to be formed in which their softening limits (Figure 5a,b) are encircled in yellow. We first placed our tip in the position i and then heated the tip up to 354 K by driving 5 mA for 4 s across the bridge structure near the tip, as in the COMSOL model, while keeping the force feedback to the tip on.

As a result of heating the paraffin surface in the vicinity of the tip, we formed the first feature indicated as i in Figure 5d. The cross-section i′ in the middle segment of Figure 5f reveals that we pulled up the surface by 10.5 nm within an area of 400 nm of diameter. Right after this, we positioned the tip in the point shown by ii and repeated the same procedure (Figure 5e). The plots in the bottom segment of Figure 5f profiles that this time, the surface raised approximately 9.5 nm toward the

DOI: 10.1021/acs.jpca.9b06056
J. Phys. Chem. A 2019, 123, 8036–8042

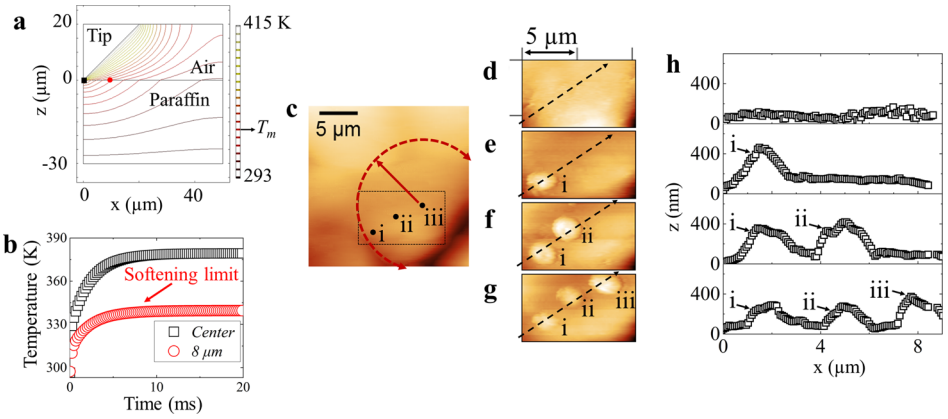

Figure 6. Similar data as in Figure 5 but with larger current through the tip, melting a much bigger area. Plots obtained from the COMSOL model representing (a) the heat dissipation from the hot tip (at 415 K) to the paraffin wax through air and (b) the instant thermal saturation of the softening limit at a radius of 8 μm, where the plots shown by the black squares and red circles represent the black and the red dots in (a). The AFM image taken from the paraffin sample show the (c) three selected positions in the operation area enclosed by the dashed lines, and the corresponding softening limit area is circled in red. AFM images taken (d) before and (e–g) after the thermomechanical pattering of the features i, ii, and iii, respectively. (h) Plots are taken from corresponding AFM images (d–g) in order to compare changing height characteristics the along z-axis before and after the patterning.

tip with approximately 400 nm of diameter again. These first results point out that the tunable thermal influence activates a well-defined mass transport. This process is repeatable in terms of the patterning size and relatively slow regarding that rising a protrusion by ~10 nm takes about 4 s.

After the observation of mass transport within the softened area, new questions arose regarding our experimental results. The first question is about the mass transport toward the emergent feature. Assuming that the material should be pulled toward the growing protrusion from its surroundings, the ditches are expected to appear around the grown protrusion. However, this is hardly noticeable in Figure 5c–e. The second question is about the ultimate size of forming a feature. In order to answer those questions, we performed further experiments. We aimed scaling up the melting area and therefore scrutinize how it effects the features formed beforehand. By observing the evolution of the shape and the size of those neighboring features, we should obtain a better understanding of the mass transport and the mechanism that pulls-off protrusions locally.

Similar to the previous case, we ran simulation with COMSOL in order to deduce the required current for scaling up the size of the softening radius. From the numerical results in Figure 6a, we can see that the temperature of the tip reaches up to 415 K by driving 7 mA across the same probe, instead of 355 K at 5 mA in the previous experiment. The temperature at the nearest point in the surface rapidly increases and saturates at 380 K. Moreover, the softening limit appears at 8 μm far from the center point (Figure 6b) this time. What stands out in Figure 6c encircled in red is the extended softening range, which in principle encloses the previously formed features as well. For that reason, we expect to observe a change in their volume by mass transport toward the emergent new feature.

Next, we performed the experiment using the calculated regimes. The AFM image in Figure 6c shows the operation area with the dashed lines enclosing the selected three positions for the features to be formed. Figure 6d represents the surface topography before the the thermomechanical process, wherein the roughness is approximately 60 nm; see the topmost section of Figure 6h. Using the set parameters applied in the model, we first formed feature-i with 2 μm of diameter, which raised ~350 nm upwards. Later on, we patterned feature-ii with 2 μm of diameter again where the local height increased ~300 nm. However, what stands out in Table 1 is that feature-i shrunk ~100 nm, while feature-ii was being formed (Figure 6f). Then, following the same process, we formed feature-iii with 2 μm of diameter and ~300 nm of height. As Table 1 reveals, feature-i and ii shrunk 80 and 140 nm, respectively, because of the mass transport toward the emergent feature-iii (Figure 6g).

Table 1. Height Evolution of the Formed Features due to the Mass Transport

	figure			
feature	5(d)	5(e)	5(f)	5(g)
i	0 nm	350 nm	250 nm	170 nm
ii	0 nm	0 nm	300 nm	200 nm
iii	0 nm	0 nm	0 nm	300 nm

The experimentally observed shrinking of the patterned features provides evidence for mass transport along a quite long distance on the thermally softened surface. It also explains why it is hard to recognize the ditches around the grown protrusion. Regarding the feature sizes formed in the last experiment and assuming that the material was taken homogeneously from the entire melt area of 16 μm in diameter, one can estimate the resulting ditch depth to be about 5 nm. This is less than the surface roughness estimated as 60 nm; therefore, it is difficult to reveal.

The absence of the expected ditches in our work also correlates with those of Lyuksyutov et al. who also formed similar features using AFMEN.[2−4] In their studies, the ditch-like structures are not visible on the polystyrene surface[2,4] in contrast to the PMMA surface.[4] To develop a full picture of the ditch occurrence, further studies can focus on that mass transport either over a less rough surface or by setting reference points around the protrusion.

As suggested above, we can characterize the mass transport in order to optimize and confine the softened area. However, another question that now comes up is whether this process can be further scaled down to sub 400 nm of diameter and to

DOI: 10.1021/acs.jpca.9b06056
J. Phys. Chem. A 2019, 123, 8036−8042

which minimal feature sizes. In order to answer this question, our results should be connected to concrete parameters of the polymer as well as the probe design. The first aspect can be attributed to determination of kinetics of protrusion formation and could depend on the rheology of the polymer system determined by surface tension forces, viscosity, melt or glass temperatures, and timing of the force application. According to Sedin and Rowlen,[19] these factors contribute to the pull-off force, generalized by the local capillary force and the van der Waals force, occurring in our process.

Although we have no adequate description determining the protrusion size, we still can speculate about the main limiting factors characterizing the growth. Under the FPP influence, heating and melting decreases the surface tension locally from 20 to 14 mN m^{-1}.[20] Therefore, the relatively low surface energy of the locally softened paraffin may facilitate capillary instability.[21] This instability, however, should be provoked by the van der Waals forces when the distance between the surface and the tip apex of FPP is periodically less than 1 nm and is expected to be more confined in the center than the melted area. For instance, our calculations in Figure 6 show that the melted area is about ~16 μm wide, which is much bigger than the formed protrusion and even bigger than the imaging area. However, the features are 2 μm wide, which is eight times smaller than the lateral size of the softened volume. This confirms our suggestion about the active role of the well-confined van der Waals forces, which yields the feature formation by a pull-off force.

On the other hand, the actual size of the protrusions comes up broader than the surface area to which the van der Waals forces are applied. This broadening may point out that the reaction of the capillary effects to the softening surface tends to increase the radii of the emergent features and serves as a limiting factor for the size of the protrusion.

In future investigations, it might be possible to scale down the present limits of feature formation by reducing the softening area. To obtain smaller features, we might exploit either shorter heat pulses in the micro-/nanosecond range or a reduced size of the heat emitting zone at the tip end by making the bridge area smaller, down to 100 nm. The realization of fast regimes of protrusion growth and use of more advanced FPP requires additional experiments, which are outside the scope of our present letter.

CONCLUSIONS

We achieved AFM-assisted polymer patterning in any selected position on a paraffin surface using a multitasking FPP. We performed thermomechanical patterning with raising features, while the hot tip was remaining in the noncontact regime. As an AFM tip, we use a planar structure with a sharp cleaved corner instead of a needle-like tip. The planar structure allows us to use standard deposition and lithography for functionalization by forming a structure on the conducting face of the probe. In this way, we can fabricate a complex nanostructure located at the tip end. We localized a strong temperature gradient very close to the surface by concentrating high current density within 0.1−10 μm across the tip end.

OUTLOOK

The achieved result provides inspiration for broadening the application of our methods. In practice, instead of mechanically plowing or thermally milling, various organic materials can be used for the 3D nanopatterning and nanoprinting by gently pulling by the tip.

Because a well-confined thermal gradient can be controlled by the FPPs without any tip-sample contact, a fundamental research of the surface kinetics and its dependency on the rheology of different polymer systems can be performed as well.

Moreover, the heat treatment by the FPP can be exploited not only for the local melting but also for initiation of much stronger processes such as decomposition, polymerization, and different kinds of chemical reactions. By a proper choice of the probe material, we can heat the tip end above 1000 K in short pulses that would be sufficient for surface tailoring of the samples from a diverse origin. Besides the high temperature itself, we also get a very high temperature gradient that can be a driving force of other mechanisms and would show effects of directed diffusion or thermal electricity on a nanoscale.

Another promising application of our approach is in addressing biological objects under AFM[22,23] but exploiting our tips with tunable well-confined heat dissipation. We could expect interesting results when using the locally heated probe to affect the wall of living cells or membranes. It would be interesting to study also reaction of viruses on the locally generated temperature gradients.

As a final application, we envision to use the current through the structured probe to generate a locally strong magnetic field at the very tip end. Because the sensitivity of the tuning fork force sensor is enough to probe weak interactions, the FPP can be used for two new types of magnetic force microscopies: MFM without permanent magnetic tips and MFM with reswitchable magnetization of the tip, which has not been achieved so far.[24]

ASSOCIATED CONTENT

Supporting Information

The Supporting Information is available free of charge on the ACS Publications website at DOI: 10.1021/acs.jpca.9b06056.

Resolution provided by the FPP (PDF)

AUTHOR INFORMATION

Corresponding Author

*E-mail: o.kurnosikov@tue.nl. Phone: +31 40 247 4307.

ORCID

H. Tunc Ciftci: 0000-0003-4422-7744

Notes

The authors declare no competing financial interest.

ACKNOWLEDGMENTS

This study is supported by STW/TTW under project number 14751. The authors thank Dr. Milan Allan and Dr. Alexey Lyulin for the fruitful discussions on intermediate results and Dr. Ivan Bykov from NT-MDT Spectrum Instruments for providing NTEGRA model AFM with a high degree of capabilities.

REFERENCES

(1) Garcia, R.; Knoll, A. W.; Riedo, E. Advanced scanning probe lithography. *Nat. Nanotechnol.* **2014**, *9*, 577−587.

(2) Lyuksyutov, S. F.; Vaia, R. A.; Paramonov, P. B.; Juhl, S.; Waterhouse, L.; Ralich, R. M.; Sigalov, G.; Sancaktar, E. Electrostatic nanolithography in polymers using atomic force microscopy. *Nat. Mater.* **2003**, *2*, 468−472.

DOI: 10.1021/acs.jpca.9b06056
J. Phys. Chem. A 2019, 123, 8036−8042

(3) Lyuksyutov, S. F.; Paramonov, P. B.; Juhl, S.; Vaia, R. A. Amplitude-modulated electrostatic nanolithography in polymers based on atomic force microscopy. *Appl. Phys. Lett.* **2003**, *83*, 4405−4407.
(4) Lyuksyutov, S. F.; Paramonov, P. B.; Sharipov, R. A.; Sigalov, G. Induced nanoscale deformations in polymers using atomic force microscopy. *Phys. Rev. B: Condens. Matter Mater. Phys.* **2004**, *70*, 1−8.
(5) Vettiger, P.; Despont, M.; Drechsler, U.; Durig, U.; Haberle, W.; Lutwyche, M. I.; Rothuizen, H. E.; Stutz, R.; Widmer, R.; Binnig, G. K. The ″Millipede″-More than thousand tips for future AFM storage. *IBM J. Res. Dev.* **2000**, *44*, 323−340.
(6) Vettiger, P.; Cross, G.; Despont, M.; Drechsler, U.; Durig, U.; Gotsmann, B.; Haberle, W.; Lantz, M. A.; Rothuizen, H. E.; Stutz, R. The "Millipede"−Nanotechnology entering data storage. *IEEE Trans. Nanotechnol.* **2002**, *1*, 39−55.
(7) Rawlings, C. D.; Zientek, M.; Spieser, M.; Urbonas, D.; Stöferle, T.; Mahrt, R. F.; Lisunova, Y.; Brugger, J.; Duerig, U.; Knoll, A. W. Control of the interaction strength of photonic molecules by nanometer precise 3D fabrication. *Sci. Rep.* **2017**, *7*, 16502.
(8) Fang, Y.; Ni, Y.; Leo, S. Y.; Taylor, C.; Basile, V.; Jiang, P. Reconfigurable photonic crystals enabled by pressure-responsive shape-memory polymers. *Nat. Commun.* **2015**, *6*, 7416.
(9) Butt, H.-J.; Berger, R.; Bonaccurso, E.; Chen, Y.; Wang, J. Impact of atomic force microscopy on interface and colloid science. *Adv. Colloid Interface Sci.* **2007**, *133*, 91−104.
(10) Novotny, L.; Stranick, S. J. Near-field optical microscopy and spectroscopy with pointed probes. *Annu. Rev. Phys. Chem.* **2006**, *57*, 303−331.
(11) Gewirth, A. A.; Niece, B. K. Electrochemical applications of in situ scanning probe microscopy. *Chem. Rev.* **1997**, *97*, 1129−1162.
(12) Siahaan, T.; Kurnosikov, O.; Barcones, B.; Swagten, H. J. M.; Koopmans, B. Cleaved thin-film probes for scanning tunneling microscopy. *Nanotechnology* **2015**, *27*, 03LT01.
(13) Chen, Y.-J.; Huang, A.; Ellingham, T.; Chung, C.; Turng, L.-S. Mechanical properties and thermal characteristics of poly(lactic acid) and paraffin wax blends prepared by conventional melt compounding and sub-critical gas-assisted processing (SGAP). *Eur. Polym. J.* **2018**, *98*, 262−272.
(14) Hida, H.; Shikida, M.; Fukuzawa, K.; Murakami, S.; Sato, K.; Asaumi, K.; Iriye, Y.; Sato, K. Fabrication of a quartz tuning fork probe with a sharp tip for AFM systems. *Sens. Actuators, A* **2008**, *148*, 311−318.
(15) Rychen, J.; Ensslin, K.; Güntherodt, H. J.; Ihn, T. Low-temperature scanning probe microscopy and magneto-transport experiments for the local investigation of mesoscopic systems combined abstract. Ph.D. Thesis, ETH Zurich, 2001.
(16) Castellanos-Gomez, A.; Agrat, N.; Rubio-Bollinger, G. Dynamics of quartz tuning fork force sensors used in scanning probe microscopy. *Nanotechnology* **2009**, *20*, 215502.
(17) González, L.; Oria, R.; Botaya, L.; Puig-Vidal, M.; Otero, J. Determination of the static spring constant of electrically-driven quartz tuning forks with two freely oscillating prongs. *Nanotechnology* **2015**, *26*, 055501.
(18) Ng, B. P.; Zhang, Y.; Wei Kok, S.; Chai Soh, Y. Improve performance of scanning probe microscopy by balancing tuning fork prongs. *Ultramicroscopy* **2009**, *109*, 291−295.
(19) Sedin, D. L.; Rowlen, K. L. Adhesion forces measured by atomic force microscopy in humid air. *Anal. Chem.* **2000**, *72*, 2183−2189.
(20) Bahadori, A. Estimation of surface tensions of paraffin hydrocarbons using a novel predictive tool approach and vandermonde Matrix. *Energy Fuels* **2011**, *25*, 5695−5699.
(21) Sullivan, D. E. Surface tension and contact angle of a liquid-solid interface. *J. Chem. Phys.* **1981**, *74*, 2604−2615.
(22) Hansma, H. G.; Hoh, J. H. Biomolecular imaging with the atomic force microscope. *Annu. Rev. Biophys. Biomol. Struct.* **1994**, *23*, 115−140.
(23) Hansma, H. G. Surface biology of DNA by atomic force microscopy. *Annu. Rev. Phys. Chem.* **2001**, *52*, 71−92.
(24) Häberle, T.; Haering, F.; Pfeifer, H.; Han, L.; Kuerbanjiang, B.; Wiedwald, U.; Herr, U.; Koslowski, B. Towards quantitative magnetic force microscopy: theory and experiment. *New J. Phys.* **2012**, *14*, 043044.

NOTE ADDED AFTER ASAP PUBLICATION

This paper was published ASAP on August 27, 2019, with an error in the Figure 4 caption. The corrected version was reposted on August 30, 2019.

DOI: 10.1021/acs.jpca.9b06056
J. Phys. Chem. A 2019, 123, 8036−8042